

Chapter 6

Quantum State Engineering of One and Two Ions

Thus far, we have discussed the ion trap and other apparatus necessary for performing quantum state engineering, investigated the interaction between the ion's spin and motional degrees of freedom, as mediated by the laser, and examined laser cooling, which gets us into the “quantum regime.” We are now ready to examine some of the ways in which these tools enable us to control the quantum state of our trapped ion(s). In this chapter, I shall discuss ways to control the motional and electronic degrees of freedom of the ion and create entanglement between them. I shall then discuss ways to characterize the complete quantum motional state. Finally, I shall discuss the creation of entanglement between two trapped ions.

6.1 Nonclassical States of Motion: One Ion

Of course, the ability to engineer various quantum states of the ion's motion does us no good whatsoever if we have no way to *verify* that we have successfully created said state. Although I will discuss methods of completely characterizing the motional state in Sec. 6.3, often it suffices to determine the P_n for the motional state: the probability that a measurement in the Fock state basis will project the state of the system onto a particular Fock state.

In other systems similar to ours (such as molecules or Rydberg atoms), the binding potential is anharmonic, so that the populations in the various potential eigenstates can

be resolved spectroscopically. However, since our system is a harmonic oscillator, it is patently *not* anharmonic, and we cannot use this technique to determine the P_n . Instead, we use the blue sideband to map motional information onto the spin state and then use the cycling transition to measure P_{\downarrow} and P_{\uparrow} , as discussed in Sec. 3.5.

6.1.1 Thermal States

There is nothing particularly nonclassical about an ion whose motion is in a thermal state. However, it is the “natural state” of a trapped ion, which normally is in thermal equilibrium with its surroundings. It is also the state in which we find the ion after optimum Doppler laser cooling, with $\bar{n} + \frac{1}{2} \approx \gamma/(4\omega)$ and \bar{n} the average vibrational quantum number. Finally, we have found that the heating discussed in Sec. 5.5 leaves the ion’s motion in a thermal state.

We may choose to express the thermal state in terms of the number state basis: from Eq. (5.1) the probability that the ion is in the motional state $|n\rangle$ is

$$P_n = \frac{\bar{n}^n}{(1 + \bar{n})^{n+1}}, \quad (6.1)$$

with $\bar{n} = (e^{\hbar\omega_m/k_B T} - 1)^{-1}$. Figure 6.1 shows the Rabi flopping curve on the upper motional sideband for a thermal state with $\bar{n} = 1.3 \pm 0.1$ [46], corresponding to a temperature of $T = 940\mu\text{K}$. The inset shows the results of a singular-valued decomposition (SVD) of the flopping curve, which extracts the various P_n . As one would expect, the distribution falls off exponentially in the Fock state number. The solid curve is a fit to the thermal distribution of Eq. (6.1), from which \bar{n} is extracted.¹

6.1.2 Fock States: Eigenstates of the Harmonic Oscillator

The Fock states $|n\rangle$ are the eigenstates of the harmonic oscillator Hamiltonian. (In the context of the formal equivalence between our system and cavity QED, the Fock

¹ Note that, as n increases, the Rabi frequencies of the different Fock state components grow closer to each other, and the error bars on the P_n grow [46]

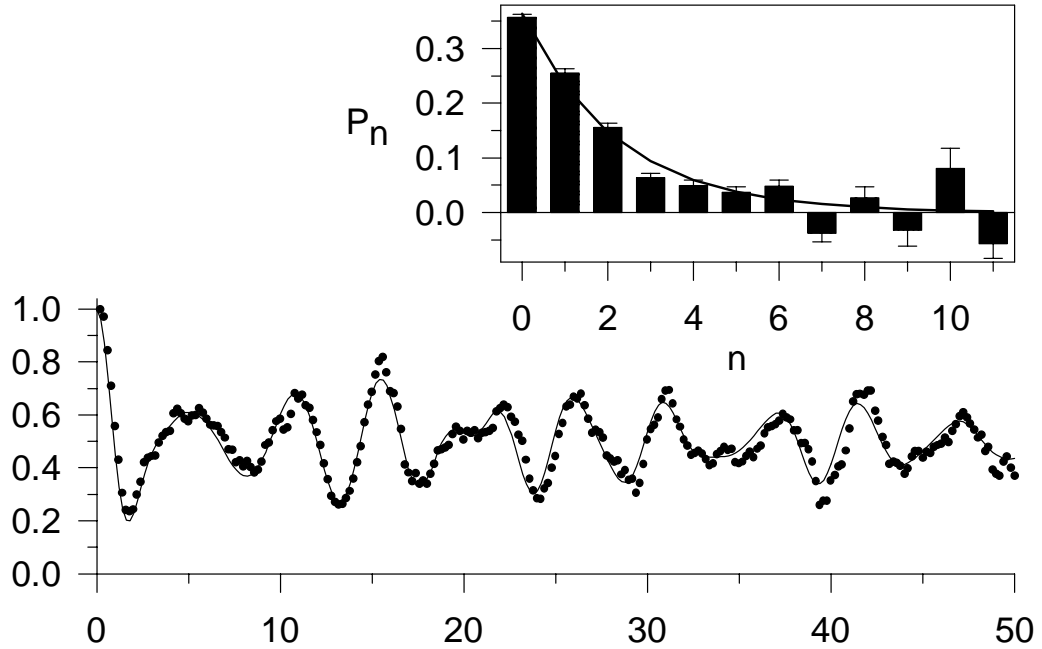


Figure 6.1: Rabi flopping curve on the blue sideband for a thermal state of the ion's motion. Different Fock state components flop sinusoidally with different Rabi frequencies (see Ch. 3), leading to the complicated dependence on the length t_{pr} of the probe pulse. The inset shows a singular-valued decomposition (SVD) of the Rabi flopping curve (see Sec. 3.5), showing the exponential distribution over the Fock states that one would expect for a thermal distribution. The solid line is a fit to a thermal distribution, yielding $\bar{n} = 1.3 \pm 0.1$.

states in the latter case give the number of photons in the cavity mode.) The Fock states are nonclassical: they are delocalized, with wave functions spread out between the corresponding classical turning points. In the position representation, the wave function of the Fock state $|n\rangle$ is given by:

$$\psi_n(z) = \left(\frac{m\omega_z}{\pi\hbar}\right)^{1/4} \frac{1}{\sqrt{2^n n!}} e^{-m\omega_z z^2/2\hbar} H_n\left(\sqrt{\frac{m\omega_z}{\hbar}} z\right). \quad (6.2)$$

The H_n 's are the Hermite polynomials [72].

The ground state of the motional mode is obtained through Raman cooling (Sec. 5.2). Starting in the ground state of motion, we can prepare $|n = 1\rangle$ by applying a π pulse on the upper motional sideband to drive $|\downarrow, n\rangle$ to $|\uparrow, n+1\rangle$. The pulse

length is required $t = \pi/(2\Omega_{0,1})$. Indeed, the minima of the curve in Fig. 3.4(b) simply correspond to interaction times such that the ion ends up in $|\uparrow, n = 1\rangle$ from $|\downarrow, n = 0\rangle$.

In order to produce higher- n Fock states, we simply use the carrier transition to return the ion to $|\downarrow\rangle$ and then apply another pulse on the upper sideband, alternating these steps until we reach the desired value of n . Alternatively, we can return the ion to $|\downarrow\rangle$ using the *lower* sideband which, if we start out in $|\uparrow\rangle$, adds another quantum of motion to the system (since the lower sideband interaction couples $|\downarrow, n\rangle \leftrightarrow |\uparrow, n - 1\rangle$). In this manner, we have created Fock states up to $|n = 16\rangle$ [46].

Similar techniques may be used to engineer superpositions of Fock states. For example, we may create the state $\frac{1}{\sqrt{2}}(|\downarrow, 0\rangle + |\downarrow, 2\rangle)$ by applying a $\pi/2$ pulse on the blue sideband followed by a π pulse on the red sideband. Such states are useful in interferometers to probe certain kinds of decoherence (see Sec. 8.2). Indeed, by applying a sequence of pulses of appropriate lengths on the carrier and motional sidebands we can, in principle, create any desired superposition of Fock states, i.e., any motional state [121]. However, for certain classes of motional states, other techniques of production exist. In the next few sections, we shall examine some of these.

6.1.3 Coherent States

A coherent state of motion $|\alpha\rangle$ [2, 94] corresponds to a displaced ground state wave packet [Eq. (6.2)] oscillating back and forth in the harmonic potential. A coherent state has the same position-momentum uncertainty product as the ground state: $\Delta\hat{z}\Delta\hat{p} = \hbar/2$. As this is the minimum value possible for this product, a coherent state is an example of a so-called “minimum uncertainty state.” For large amplitudes $|\alpha|$ of oscillation, the zero-point width is much smaller than the amplitude of motion, and the coherent state approximates a point object moving in a harmonic well; for this reason, coherent states are also called “quasi-classical states” [2], and provide a means to draw a correspondence between the quantum and classical behaviour of a particle in a har-

monic well. They are also of interest because they represent the quantized harmonic oscillator of one mode of the electromagnetic field as produced by a laser [2].

Mathematically, coherent states are those for which the ensemble averages $\langle \hat{z} \rangle$ and $\langle \hat{p} \rangle$ of the position and momentum operators follow the same equations of motion as the classical position and momentum, and for which the expectation value of the energy is equal to that of the corresponding classical particle. This is mathematically equivalent (see Ref. [2], §G_V) to the statement that $|\alpha\rangle$ are eigenstates of the operator \hat{a} : $\hat{a}|\alpha\rangle = \alpha|\alpha\rangle$. This leads to the expression

$$|\alpha\rangle = e^{-|\alpha|^2/2} \sum_{n=0}^{\infty} \frac{\alpha^n}{\sqrt{n!}} |n\rangle. \quad (6.3)$$

Note that this is a Poisson distribution over the Fock states. Physically, α gives the “size” of the coherent state: for example, $\langle z \rangle = 2z_0 \text{Re}(\alpha)$.

From a theoretical standpoint, coherent states are produced from the harmonic oscillator ground state through the action of the unitary displacement operator $\hat{D}(\alpha) = \exp(\alpha \hat{a}^\dagger - \alpha^* \hat{a})$. It is straightforward to use the Baker-Hausdorff formula to prove that $\hat{D}(\alpha)|0\rangle = |\alpha\rangle$. This is the origin of the displacement operator’s name: $\hat{D}(\alpha)$ “displaces” the ground state wave packet from the origin of the $\{z, ip\}$ plane by α . Physically, we may realize the displacement operator by applying an electric field to the ion which is oscillating at the trap frequency. If we write the field as $E = \mathbf{e}_z E_z \sin(\omega t - \phi)$, then the interaction Hamiltonian between the field and the ion’s charge is given in the interaction picture by

$$\hat{H}_I(t) = -QE_z z_0 (\hat{a} e^{-i\omega_z t} + \hat{a}^\dagger e^{i\omega_z t}) \sin(\omega t - \phi). \quad (6.4)$$

If we express the sin function in exponential form, make a rotating wave approximation and set $\omega = \omega_z$, we obtain the time evolution operator:

$$\hat{U}(t) = e^{(\Omega_d t) \hat{a}^\dagger - (\Omega_d t)^* \hat{a}} = \hat{D}(\Omega_d t), \quad (6.5)$$

where I have defined $\Omega_d \doteq -QE_z z_0 e^{i\phi} / (2\hbar)$.

We may also effectively realize the displacement operator by applying a “walking standing wave” of light which resonantly drives the ion’s motion through the optical dipole force. In order to do this, we turn on the Raman beams such that their difference frequency is equal to ω_z (rather than $\omega_0 \pm \omega_z$, as is usually the case). The light field polarizes the ion’s electron cloud, and the beat note between the two beams then drives the ion’s motion through the interaction with the induced dipole moment. One may analyze the interaction in the same manner as in Sec. 3.3. For example, if we consider the interaction between $|\downarrow\rangle$ and $|v\rangle$ induced by the Raman lasers (with $\Delta\mathbf{k}\parallel\mathbf{z}$), and adiabatically eliminate $|v\rangle$, we obtain [73]:

$$\begin{aligned} \dot{C}'_{\downarrow,n} &= i \frac{|g_1|^2 + |g_2|^2}{\Delta_R} C'_{\downarrow,n} \\ &- \sum_m \langle n | \left[\Omega^* \exp\left(i\eta(\hat{a}e^{-i\omega_z t} + \hat{a}^\dagger e^{i\omega_z t})\right) e^{-i\delta t} + H.C. \right] | m \rangle C'_{\downarrow,m}. \end{aligned} \quad (6.6)$$

As in Eq. (3.24), the first term represents an overall Stark shift of $|\downarrow\rangle$. If we absorb this into the definition of the ground state energy, then the dynamics of the $C'_{\downarrow,n}$ are the same as those obtained in the interaction picture with the Hamiltonian

$$\hat{H}_I = \hbar\Omega^* \exp\left(i \left[\eta(\hat{a}e^{-i\omega_z t} + \hat{a}^\dagger e^{i\omega_z t} - \delta t) \right]\right) + H.C. \quad (6.7)$$

If we make a rotating wave approximation, expand the exponentials of the operators \hat{a} and \hat{a}^\dagger , and assume we are in the Lamb-Dicke limit, this gives the time evolution operator

$$\hat{U}(t) = e^{(\eta\Omega^*t)\hat{a}^\dagger - (\eta\Omega t)\hat{a}} = \hat{D}(\eta\Omega^*t). \quad (6.8)$$

The above derivation is somewhat mathematical, and it is easy to lose sight of the fundamental physics in the situation. To try and identify this physics, we must remember that the two Raman beams are far-detuned from the virtual level $|v\rangle$, so that they do not drive much of the atomic population from $|\downarrow\rangle$ to $|v\rangle$. Instead, their primary effect on the atom is to produce an energy shift of the atomic levels through the AC Stark effect. In order to examine this shift, we may use time-dependent perturbation

theory to calculate the energy of the part of the state vector left in $|\downarrow\rangle$ (the eigenstate of the free Hamiltonian of the atom's spin degree of freedom). This is given by

$$\begin{aligned} \langle \downarrow | \hat{H}_{int} | \psi(t) \rangle &\approx \langle \downarrow | \hat{H}_{int} | \psi^{(1)}(t) \rangle \\ &\approx \langle \downarrow | \hat{H}_{int} [|\downarrow\rangle + c_v^{(1)}(t) |v\rangle], \end{aligned} \quad (6.9)$$

where the superscripts refer to first-order expansion perturbation theory solutions.

Now, assuming that the ion is illuminated equally by two plane waves travelling in the z -direction, the total electric field experienced by the ion is given by:

$$\begin{aligned} \mathbf{E} &= \mathbf{e}_x E (\cos(k_1 z - \omega_{L1} t + \phi_1) + \cos(k_2 z - \omega_{L2} t + \phi_2)) \\ &= \mathbf{e}_x 2E \cos(k_{avg} z - \omega_{avg} t + \phi_{avg}) \cos\left[\frac{1}{2}(\Delta k z - \delta t + \delta\phi)\right]. \end{aligned} \quad (6.10)$$

In the first cosine term, the *avg* subscripts refer to the averages of the laser wave-vectors, frequencies, and phases. This term is very rapidly varying. The second cosine term, however, is slowly-varying. Thus, we may express H_{int} as:

$$H_{int} = -2g(t) \left[e^{i(k_{avg} z - \omega_{avg} t + \phi_{avg})} + e^{-i(k_{avg} z - \omega_{avg} t + \phi_{avg})} \right], \quad (6.11)$$

where

$$g(t) \doteq \langle \downarrow | \mathbf{e}_x \cdot \mathbf{r}_{el} \frac{eE}{2\hbar} \cos\left[\frac{1}{2}(\Delta k z - \delta t + \delta\phi)\right] | v \rangle \quad (6.12)$$

is a coupling strength which varies slowly in time. Substituting this interaction Hamiltonian into the usual time-dependent perturbation theory expansion, we find that (Schrödinger picture):

$$C_v^{(1)}(t) = \frac{-2g^*(t)e^{ik_{avg}z}}{\omega_{avg} - \omega_{v,\downarrow}} \left(e^{-i\omega_{avg}t} - e^{i\omega_{v,\downarrow}t} \right). \quad (6.13)$$

Finally, if we plug this into Eq. (6.9) and make a rotating wave approximation, we obtain:

$$\langle \downarrow | \hat{H}_{int} | \psi(t) \rangle = \frac{4|g(t)|^2 \hbar}{\omega_{v,\downarrow} - \omega_{avg}} \left[e^{-i(\omega_{v,\downarrow} - \omega_{avg})t} - 1 \right], \quad (6.14)$$

where ϵ_{\downarrow} is the unperturbed energy of $|\downarrow\rangle$. Now, $\omega_{v,\downarrow} - \omega_{avg} = \Delta_R - \frac{1}{2}\delta \approx \Delta_R$. Thus, averaging over the fast time scale $1/\Delta_R$, we have

$$\langle \downarrow | \hat{H}_{int} | \psi(t) \rangle \approx -\frac{4\hbar |g(t)|^2}{\Delta_R}. \quad (6.15)$$

So the effect of the “standing walking wave” is to create a time-dependent Stark shift of the level $|\downarrow\rangle$. The time dependence occurs in the term $|g(t)|^2$ and thus, at the frequency $\delta \approx \omega_z$. This time-dependent Stark shift leads to a time-dependent force on the ion which, in the Lamb-Dicke limit, acts like a displacement operator upon the ion. Although the effects on $|\downarrow\rangle$ have been treated here, $|\uparrow\rangle$ is affected in a similar way.

The “walking standing wave” technique has the following advantage: the force produced by this interaction depends on the polarization of the lasers and the matrix elements of the atomic levels. So, for example, if the Raman beams are polarized σ^- then, since there is no $|F = 2, m_F = -(2 + 1)\rangle$ virtual state in the $2p \ ^2P_{1/2}$ level to which $|\downarrow\rangle$ may couple, only the $|\uparrow\rangle$ state is affected by the Raman beams. This allows us to create a coherent state *only* in the component of the ion’s state vector which is in $|\uparrow\rangle$, which is useful for interferometry or for producing “Schrödinger cat” states. I shall discuss these issues in greater detail in Sec. 6.2.1.

Fig. 6.2(a) shows the Rabi flopping curve on the upper sideband for a coherent state with $|\alpha| = 3.1 \pm 0.1$ [46]. Notice the so-called “collapse” and “revival” in P_1 : the Rabi flopping collapses to almost a straight (50%) line around time $t = 8\mu s$, but then coherent features reappear (“revive”) at around $t_{pr} = 15\mu s$. These features are characteristic of coherent states [122, 123], and are a result of the strongly peaked Poisson distribution of Fock states which make up a coherent state.

6.1.4 Squeezed States

A coherent state is one example of a “minimum-uncertainty state.” For this state, $\Delta\hat{z} = \sqrt{\frac{\hbar}{2m\omega_z}}$ and $\Delta\hat{p} = \sqrt{\frac{m\hbar\omega_z}{2}}$, so that $\Delta\hat{z}\Delta\hat{p} = \hbar/2$. However, it is possible to create

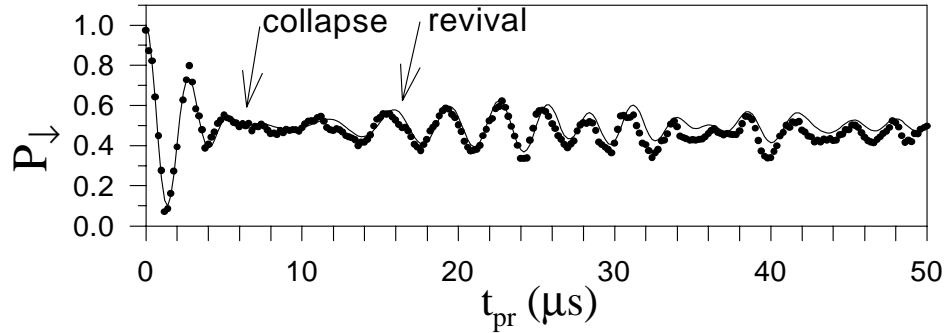


Figure 6.2: Rabi flopping curve for a coherent state, with $|\alpha| = 3.1 \pm 0.1$. The “collapse” and “revival” characteristic of such a state are evident. The solid curve is a fit to a coherent state population distribution (yielding $|\alpha| = 3.1 \pm 0.1$ for the fit).

states such that $\Delta \hat{z} < \sqrt{\frac{\hbar}{2m\omega_z}}$ at the expense of increasing $\Delta \hat{p}$ commensurately, or vice versa. Such states are called “squeezed states” [124]. If we picture the ion’s wave packet in the $\{z, p\}$ plane then, roughly speaking, a coherent state forms a circular disk (of finite “radius” to satisfy Heisenberg) a distance $|\alpha|$ from the origin. A squeezed state is an ellipse — a squeezed circle, if you will.

Mathematically, squeezed states are produced from the ground state of motion through the action of the unitary “squeeze operator”² $\hat{S}(\epsilon) = \exp[\frac{1}{2}(\epsilon^* \hat{a}^2 - \epsilon (\hat{a}^\dagger)^2)]$ where, in the traditional nomenclature, ϵ is expressed as $\epsilon = R e^{2i\phi}$. One can show [105] that $\hat{S}^\dagger(\epsilon)(\tilde{z} + i\tilde{p})\hat{S}(\epsilon) = \hat{y}_1 e^{-R} + i\hat{y}_2 e^R$, where $\hat{y}_1 + i\hat{y}_2 = (z + ip)e^{-i\phi}$. Thus, the squeeze operator causes a rotation in the $\{z, p\}$ plane by angle ϕ , then attenuates one component of the motion as it amplifies the other. This leads to $\Delta \hat{y}_1 = e^{-R}$ and $\Delta \hat{y}_2 = e^R$, so that indeed, the squeezed state features reduced uncertainty in one quadrature at the expense of increased uncertainty in the other.

² Actually, in full generality, a squeezed state is produced by $\hat{D}(\alpha)\hat{S}(\epsilon)$ acting on the vacuum, rather than only $\hat{S}(\epsilon)$. This is a squeezed state which is displaced from the origin of the $z - p$ plane. What I am referring to as “squeezed states” are, to be more accurate, actually called “squeezed vacuum states.”

We can create squeezed states by modulating the strength of the trap at twice the trap frequency. This produces a parametric resonance (much like the parametric resonance one uses to get oneself going when one is sitting on a swing!), which produces a squeezed state of motion [125]. However, this technique is not practical with our apparatus: since we would like to modulate the strength of the trap, we require strong field gradients at frequency $2\omega_z$ (see Ch. 2), but frequency components at $2\omega_z$ are heavily attenuated by the filters on the trap.

Instead, we use the same “walking standing wave” technique used to produce coherent states. This time, we set the detuning δ of the laser beams to be equal to $2\omega_z$. Now in Eq. (6.7), $\delta = 2\omega_z$, and if we are in the Lamb-Dicke limit and make a rotating wave approximation (neglecting off-resonant terms), the result is that

$$\hat{H}_I = \frac{\hbar\eta^2}{2} \left[\Omega^* \hat{a}^2 + \Omega (\hat{a}^\dagger)^2 \right], \quad (6.16)$$

leading to

$$\hat{U}(t) = e^{\frac{1}{2}[(i\eta^2\Omega)^* \hat{a}^2 - (i\eta^2\Omega)(\hat{a}^\dagger)^2]t} = \hat{S}(i\eta^2\Omega t) \quad (6.17)$$

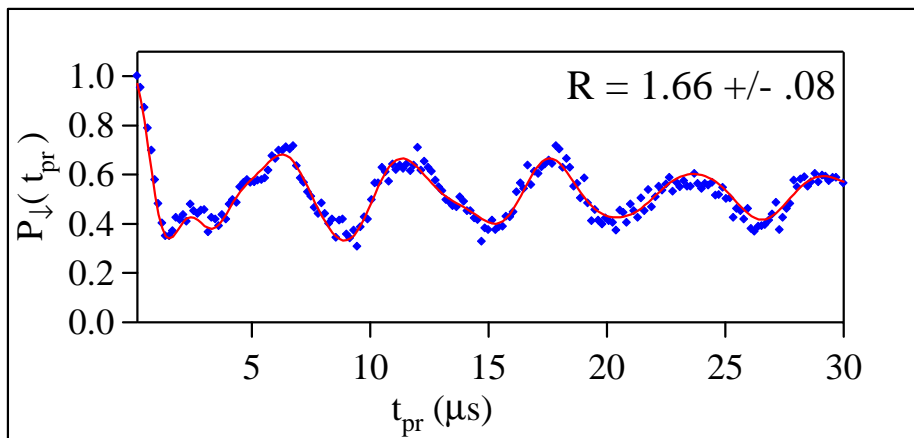
(where the laser phase is included in Ω).

Figure 6.3(a) shows the Rabi flopping curve on the blue sideband for a squeezed state with $R \approx 1.5$. Figure 6.3(b) shows the result of leaving the lasers on for a longer period of time. In this latter case, the ion is driven out of the Lamb-Dicke regime, and the higher-order terms in Eq. (3.7) come into play. The resulting state is no longer a pure squeezed state, but suffers additional rotation and shearing in the $\{z, p\}$ plane.

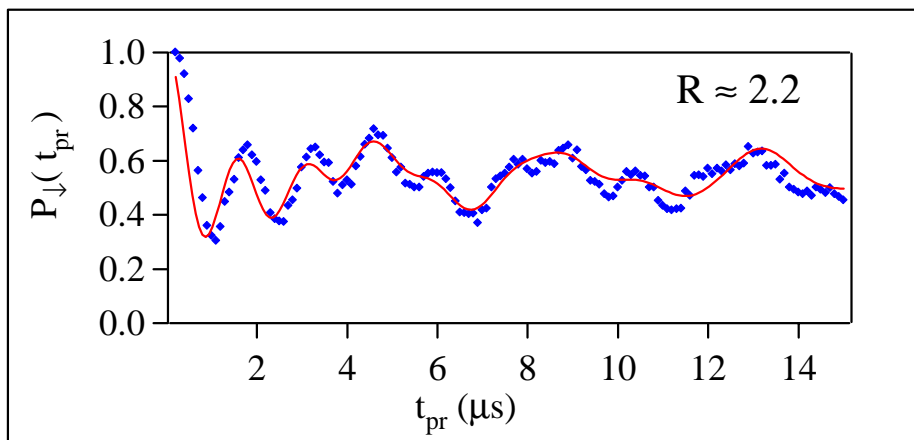
6.2 Entangling Spin and Motion: One Ion

6.2.1 “Schrödinger’s Cat”

The phrase “Schrödinger’s cat” refers to a paradoxical *Gedankenexperiment* [9] in which Schrödinger envisioned correlating the state of a macroscopic object with that of a microscopic one (which obeys quantum mechanics). In particular, he imagined a



(a)



(b)

Figure 6.3: (a) Rabi flopping curve for a squeezed state, with $R = 1.5 \pm .2$. (b) Rabi flopping curve for a state in which the parametric, “walking standing wave” interaction is left on long enough for nonlinearities to enter the expressions for the Rabi frequencies. The solid curves are fits to the squeezed state population distribution.

cat to be confined inside a box with a radioactive nucleus, a bottle of cyanide, and a trigger device which would break the bottle if the nucleus decayed — thus killing the cat. The paradox arises in the case when the nucleus is in a superposition of decayed and undecayed. Although we are used to considering such a situation, in this case it poses a problem. For, if we consider the system as a whole quantum mechanically then, since the cat’s state is correlated with that of the nucleus, we are left with a situation in which, according to the standard interpretation of quantum mechanics, we must consider the cat to be in a superposition of being alive *and* dead. This is not a state in which cats are normally found!

This paradox was meant to highlight some of the difficulties with the traditional Copenhagen interpretation, which drew an (arbitrarily placed) dividing line between the microscopic world of quantum mechanics and the macroscopic world which we experience. Much discussion has ensued on the subject of Schrödinger’s hapless feline, but the *Gedankenexperiment* illustrates the general lack of agreement on exactly how the transition from quantum mechanical to classical behaviour occurs.

In the context of quantum optics, the phrase “Schrödinger’s cat” was appropriated to describe a situation in which a microscopic degree of freedom is entangled with a mesoscopic one. We use the term in the same vein in the context of our trapped-ion system, to describe the situation in which the atom’s spin is entangled with two mesoscopically distinct motional states. In particular, such states provide a controlled environment for studying quantum decoherence, which may shed light on the issue of “wave function collapse” [15] and also is of interest to us in our examination of quantum computation (see Sec. 7.1).

In particular, we can create the state [47]

$$|\Psi\rangle = \frac{1}{\sqrt{2}}(|\downarrow, \alpha_1\rangle + |\uparrow, \alpha_1\rangle), \quad (6.18)$$

where $|\alpha_j\rangle$ is a coherent state of motion. If, for example, $|\alpha_\uparrow\rangle = |-\alpha_\downarrow\rangle$, then we have a situation when, at the extremum of the ion's motion, it is (in some sense) *simultaneously* in the state $|\downarrow\rangle$ and at one side of the trap and in the state $|\uparrow\rangle$ and at the *opposite* side of the trap! We have created such a state where the two coherent state wave packets were separated by 80 nm, about ten times the width of the wave packet.

In order to create such a state, we take advantage of the “walking standing wave” method of generating coherent states. As mentioned in Sec. 6.1.3, the interaction between the laser beams and the ion depends on the ion's electronic state (different electronic states have different matrix elements — see Appendix B). So, for example, if the light is polarized σ^- then, since there is no $2p\ ^2P_{1/2}, m_F = -3$ level with which $|\downarrow\rangle$ can interact, the lasers only affect $|\uparrow\rangle$ (at least, if we ignore off-resonant transitions through the $2p\ ^2P_{3/2}$ level). To create the state $\frac{1}{\sqrt{2}}(|\downarrow\rangle + |\uparrow\rangle)$, we could turn on the “walking standing wave”, exchange $|\uparrow\rangle$ and $|\downarrow\rangle$, and repeat the process. This was the technique used in Ref. [47].

However, there is a simpler technique for producing states of the form $|\Psi\rangle$. If we arrange the polarizations of the two laser beams correctly, then we can drive both $|\downarrow\rangle$ and $|\uparrow\rangle$ at the same time. In practice, the RR_{co} beam must have the polarization $\frac{1}{\sqrt{2}}(\sigma^+ + \sigma^-)$, since it is put into the trap with a polarizing beamsplitter cube. Let the RR_\perp beam have the polarization $\Lambda\sigma^- + \Upsilon\sigma^+$. Assume that $g_1 = g_2 = g$. Then, including the matrix elements between $|\downarrow\rangle$, $|\uparrow\rangle$, and the $2p\ ^2P_{3/2,1/2}$ states explicitly (see Appendix B), the effective Rabi frequencies when we turn on the displacement beams are

$$\Omega_\downarrow = \frac{g^2}{\Delta_R + \omega_0} \frac{2\Upsilon}{3} + \frac{g^2}{\Delta_R + \delta_{FS} + \omega_0} \left(\Lambda + \frac{\Upsilon}{3} \right) \quad (6.19)$$

$$\Omega_\uparrow = \frac{g^2}{\Delta_R} \left(\frac{\Lambda}{2} + \frac{\Upsilon}{6} \right) + \frac{g^2}{\Delta_R + \delta_{FS}} \left(\frac{\Lambda}{2} + \frac{5\Upsilon}{6} \right). \quad (6.20)$$

In these equations, δ_{FS} is the fine-structure splitting of the $2p\ ^2P$ levels (≈ 197 GHz). It is convenient to set $|\Lambda| = |\Upsilon|$ when running the experiment, for then the Stark shifts

of the two levels ($|\downarrow\rangle$ and $|\uparrow\rangle$) are the same (up to order δ_{HF}/Δ_R). To get a rough idea of the effects of the two beams on the different atomic levels, assume that we are tuned near the $2p\ ^2P_{1/2}$ level, so that we may neglect the second terms in Eqs. (6.19) and (6.20). Let us also neglect ω_0 with respect to Δ_R . If we assume that Λ is purely real, then we may write $\Upsilon = \Lambda e^{2i\chi}$. (For example, we may alter the polarization of the RR_\perp beam with a half-wave plate. In this case, χ is the angle of said wave plate from the vertical, which is 90° from the plane of the Blue Raman polarization.) Making these substitutions, we find that:

$$\frac{\Omega_\downarrow}{\Omega_\uparrow} \approx \frac{4}{1 + 3e^{-2i\chi}}. \quad (6.21)$$

Since α is proportional to Ω_j , we can vary $\alpha_\downarrow/\alpha_\uparrow$ by varying the laser beam polarization. Fig. 6.4 shows $\Omega_\downarrow/\Omega_\uparrow$ as a function of the angle of the aforementioned polarizer. In practice, we usually chose to have $\alpha_\downarrow = -2\alpha_\uparrow$.

Thus, in order to create a state of the form Ψ , we apply a $\pi/2$ -pulse on the co-propagating carrier, to create $\frac{1}{\sqrt{2}}(|\downarrow\rangle + |\uparrow\rangle)$, then turn on the displacement laser beams, creating Ψ with only one displacement pulse. If $|\alpha|$ were large enough, we could, in principle, spatially resolve the two wave packets and correlate the atom's position with its electronic state [126]. However, this is not possible for the size of cats which we produced (which really, given their size, were more like kittens than cats).

Instead, we interfere the motional wave packets in $|\uparrow\rangle$ and $|\downarrow\rangle$, to produce interference fringes. In order to do this, we reverse the original carrier and displacement pulses to reverse the state creation. However, we put a variable phase between the first displacement pulse and the reversal pulse (by putting a phase shift on the rf driving the splitter AOM). As this phase is swept, a pattern of fringes appears in P_\downarrow . Thus, the complete experiment is really a form of Ramsey-type interferometer (see Sec. 3.4 or Ref. [95]). The first carrier and displacement pulses create a superposition state, playing the role of the first Ramsey zone. Similarly, the reversal pulses, which have a

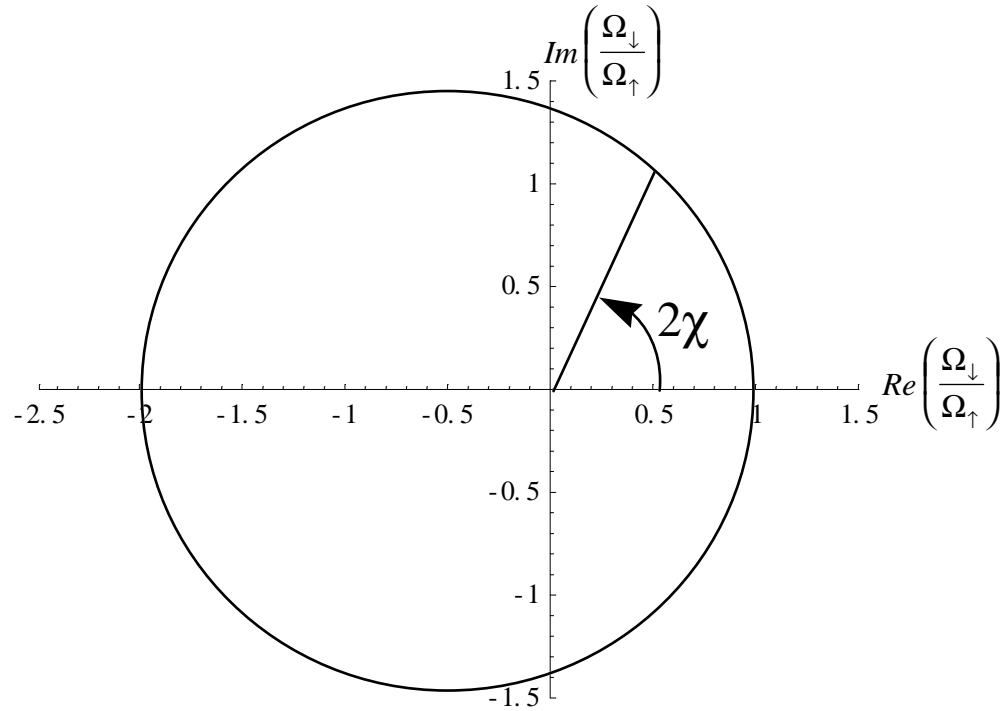


Figure 6.4: $\frac{\Omega_{\downarrow}}{\Omega_{\uparrow}}$ as a function of the angle of the polarizer in the RR_{\perp} beam line from the vertical. This assumes that $\alpha_{\uparrow} = 1$, that $|\Upsilon| = |\Lambda|$, and neglects the ground-state hyperfine splitting. By varying the polarizer angle, we can vary the relative displacements of $|\downarrow\rangle$ and $|\uparrow\rangle$ produced by the “walking standing wave” interaction, and produce “Schrödinger cat” states.

different effective phase than the first pulses, play the role of the second Ramsey zone.

We shall return to this idea in Ch. 8.

As a function of the phase ϕ between the state creation and reversal (and assuming equal Rabi frequencies on the creation and reversal pulses), P_{\downarrow} is given by:

$$P_{\downarrow}(\phi) = \frac{1}{2} \left(1 + e^{-|\alpha_{\downarrow} - \alpha_{\uparrow}|^2 (1 + \cos \phi)} \times \cos \left[\vartheta + 2(1 + \cos \phi) \text{Im}\{\alpha_{\downarrow}^* \alpha_{\uparrow}\} + \sin \phi (|\alpha_{\downarrow}|^2 - |\alpha_{\uparrow}|^2) \right] \right), \quad (6.22)$$

where α_{\downarrow} and α_{\uparrow} are the coherent state amplitudes in $|\downarrow\rangle$ and $|\uparrow\rangle$ produced by the state creation, and ϑ allows for the possibility of a phase between the two carrier $\pi/2$

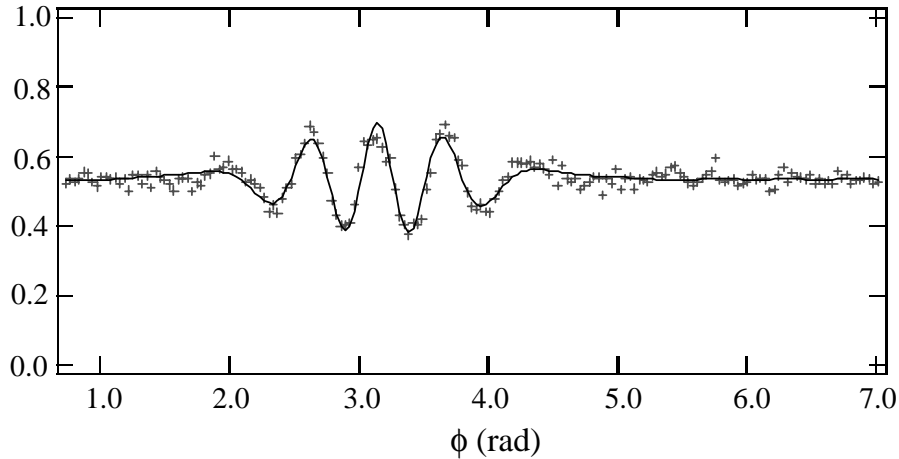


Figure 6.5: Measured and fit interference signals $P_{\downarrow}(\phi)$ for a “Schrödinger cat” state [see Eq. (6.18)], as a function of the phase ϕ between coherent state creation and reversal. For this data, one of the spin states was displaced while the other was not. The solid line is a fit to theory.

pulses. Characteristic interference patterns are shown in Fig. 6.5 — they indicate the correlations and coherence inherent in the state.³

The creation of Schrödinger cat states with trapped ions is paralleled in systems such as atom [127, 128, 129, 130], electron [131], or neutron [132] interferometers or in Rydberg states in atoms [133, 134, 135]. However, in our case, there is no dispersion of the wave packet with time, since the confining potential is harmonic. This provides a well controlled system with which to study, for example, decoherence. I shall return to this in Ch. 8.

6.3 Determining the Complete Motional State

One of the more significant changes in our concept of the physical universe wrought by quantum mechanics is the lack of distinction between measurement and

³ The data in Ref. [47] were taken in a slightly different manner: only one displacement pulse was used, and the phase of the second $\pi/2$ pulse was swept.

state preparation. In our case, for example, the same Raman interactions that we use to create motional states are also used to map information about the motional-level populations onto the ion’s spin, which is our observable. The fact that the Rabi frequency on the motional sidebands depends on the motional level allows us to discriminate different Fock state components with unit efficiency (by, for example, a singular-value decomposition [96] of the frequency components of the Rabi flopping curve), as discussed in Sec. 3.5.

This technique allows us to determine the n -state populations (or probabilities), but does not give us phase information; therefore, it does not provide us with a *complete* description of the motional states. However, by using a coherent state generation interaction — which is equivalent to a displacement in phase space — in conjunction with the Rabi flopping curves, we can reconstruct the Wigner function or the density matrix of the motional state [136]. The techniques we use are similar to those of quantum state tomography [48].

Like the density matrix, the Wigner function [137] provides a complete description of a quantum state. It is a description formulated in phase space — the same phase space familiar from classical mechanics. However, the Heisenberg Uncertainty Principle prohibits us from simultaneously specifying both position and momentum, so we must make some modifications to our classical picture of phase space and phase space probability distributions. The Wigner function $W(z, ip) \equiv W(\alpha)$ (where $\alpha = z + ip$) is the “best possible phase space distribution” [138]:

$$W(\alpha) \equiv W(z, ip) = \frac{1}{2\pi} \int_{-\infty}^{+\infty} e^{ipq} \left\langle z - \frac{q}{2} \left| \rho \right| z + \frac{q}{2} \right\rangle dq. \quad (6.23)$$

(Here ρ is the motional state density matrix.) However, the “weirdness” of quantum mechanics gives it some unusual properties for a probability distribution: it can, for example, be negative! For this reason, it is usually referred to as a “quasiprobability distribution.” Nonetheless, for a given state, the Wigner function does give the correct

marginal distributions for z and p (as we would calculate from $\langle z \rangle$ or $\langle p \rangle$). For example:

$$\langle z | \rho | z \rangle = \int_{-\infty}^{+\infty} W(z, ip) dp > 0. \quad (6.24)$$

The basic idea for determining the density matrix ρ or the Wigner function $W(\alpha)$ is to measure the overlap of the motional state with some known set of basis functions — in our case, the Fock states. If we displace the motional states by different amounts and in different directions in phase space, we can measure how the overlap with the Fock states changes with the (phase-dependent) displacement and thus extract phase, as well as amplitude, information.

If we represent the initial motional state as $|\psi\rangle = \sum_{n=0}^{\infty} C_n |n\rangle$, then the first step in determining the Wigner function is to displace this state using a resonant electric field at the motional frequency (see Sec. 6.1.3). After the displacement, the motional state $|\psi_d\rangle$ is now given by $|\psi_d\rangle = \sum_{n=0}^{\infty} C_n(\alpha) |n\rangle$, where the expansion coefficients $C_n(\alpha)$ explicitly depend on the displacement. If a Raman probe pulse on the upper motional sideband is then applied, the signal is given by (see Eq. (3.34)):

$$P_{\downarrow}(t_{pr}, \alpha) = \sum_{n=0}^{\infty} |C_n(\alpha)|^2 \cos^2(\Omega_{n,n+1} t_{pr}). \quad (6.25)$$

From this, the coefficients $|C_n(\alpha)|^2$ (which are simply the P_n 's of the displaced motional state) can be determined by performing a singular-valued decomposition. The Wigner function at the point $\alpha = z + ip$ in phase space is then given by the simple formula [139, 140, 141, 142]:

$$W(\alpha) = \frac{2}{\pi} \sum_{n=0}^{\infty} (-1)^n |C_n(\alpha)|^2. \quad (6.26)$$

In practice, we truncate the sum at some n_{max} . Fig. 6.6(a) shows the reconstructed Wigner function for an approximate $|n = 1\rangle$ Fock state; the negative values near the origin indicate the highly nonclassical nature of the state. Fig. 6.6(b) shows the reconstructed Wigner function of a coherent state. The theoretically predicted Wigner function is a two-dimensional Gaussian, and the reconstructed Wigner function, indeed, appears Gaussian.

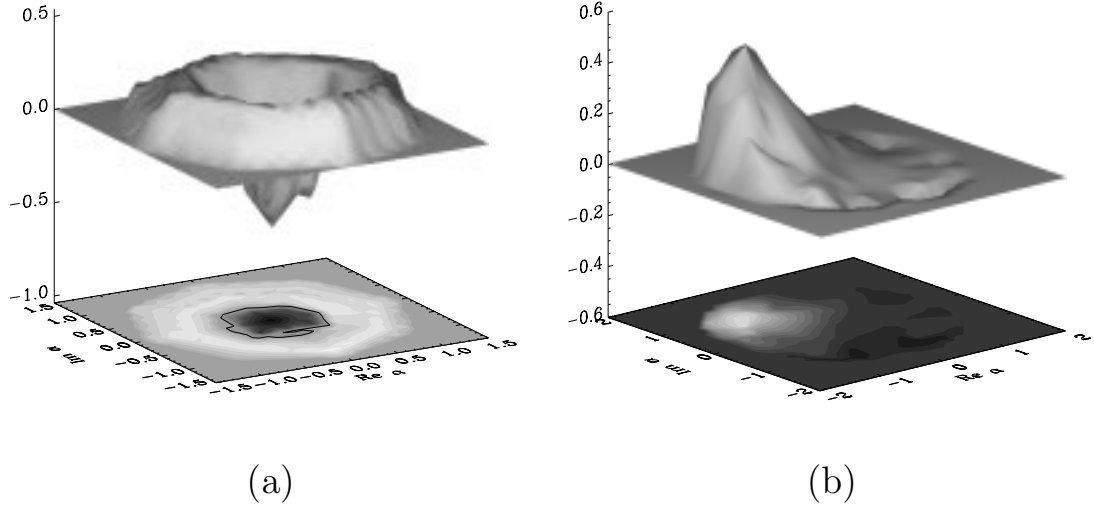


Figure 6.6: (a) Reconstructed Wigner function for an $|n = 1\rangle$ Fock state. The plotted points are the result of fitting a linear interpolation between the actual data points to a 0.1 by 0.1 grid. The octagonal shape is an artifact of the eight measured phases per radius (ten radii were measured). The white contour represents the line $W(\alpha) = 0$. The negative values around the origin highlight the nonclassical nature of this state. (b) Reconstructed Wigner function for a coherent state $|\alpha\rangle$. The points are the fit of a linear interpolation of the data points to a 0.13 by 0.13 grid. The approximately Gaussian minimum-uncertainty wave packet is centred around an amplitude of 1.5 (from the origin). The half-width at half maximum is ≈ 0.6 , in accordance with the minimum uncertainty half width of ≈ 0.59 . To suppress artifacts in the Wigner function summation, data with $n_{max} = 5, 6$ have been averaged together (as suggested by M. Collett, *private comm.*).

This technique gives the Wigner function at a particular point in phase space: in order to map out the motional state with a given precision, a suitably large number of measurements is required. It is also possible to make $2N$ measurements and completely reconstruct the density matrix elements ρ_{nm} with respect to the Fock states up to $n = m = M - 1$. To do this, we displace the state to be measured to $2M$ different locations in phase space equally spaced along a circle of radius $|\alpha|$, each time measuring the Rabi flopping curve. This allows us to invert the relationship

$$|\mathcal{C}_n(\alpha)|^2 = \langle n | \hat{D}^\dagger(\alpha) \hat{\rho} \hat{D}(\alpha) | n \rangle, \quad (6.27)$$

where $\hat{D}(\alpha)$ is the unitary operator representing the displacement interaction. (In practice, since the data over-constrained the relationship, we used a fitting procedure instead of an inversion.) Note that $|\mathcal{C}_0(\alpha)|^2/\pi$ is the Q -function [105]. The details are described in Refs. [136, 48] and a similar technique is described in Ref. [143]. However, I shall briefly outline the idea of the technique here. Write $|\mathcal{C}_n(\alpha)|^2 = Q_n(\alpha)$. Then, using the fact that $\hat{a}^n e^{-\alpha\hat{a}^\dagger} = \hat{a}^{n-1} e^{-\alpha\hat{a}^\dagger} (\hat{a} - \alpha)$, and applying the properties of \hat{a} and \hat{a}^\dagger , we can rewrite Eq. (6.27) as

$$Q_n(\alpha) = \frac{e^{-|\alpha|^2} |\alpha|^{2n}}{n!} \sum_{l,m=0}^{\infty} \sum_{j,j'=0}^n \frac{(\alpha^*)^{l-j} \alpha^{m-j'}}{l!m!} (-1)^{-j-j'} \\ \times \binom{n}{j} \binom{n}{j'} \sqrt{(m+j)!(l+j)!} \rho_{l+j',m+j}. \quad (6.28)$$

Now, suppose that we measure $Q_n(\alpha)$ with α equally spaced on a circle: $\alpha_p = a e^{i(\pi/M)p}$, with $p \in \{-M, \dots, M-1\}$. Then, Eq. (6.28) becomes

$$Q_n(p) = \frac{e^{-a^2} a^{2n}}{n!} \sum_{l,m=0}^{\infty} \sum_{j,j'=0}^n \frac{a^{l+m-j-j'}}{l!m!} (-1)^{-j-j'} \\ \times \binom{n}{j} \binom{n}{j'} \sqrt{(m+j)!(l+j)!} \rho_{l+j',m+j} e^{ip(\pi/M)(j+m-l-j')}. \quad (6.29)$$

One can then determine $\rho_{n,m}$ by use of the following orthonormality relationship:

$$\frac{1}{2M} \sum_{p=-M}^{M-1} e^{ip(\pi/M)r} e^{-ip(\pi/M)s} = \delta_{r,s}. \quad (6.30)$$

So, if we multiply Eq. (6.29) by $\frac{1}{2M} e^{-ip(\pi/M)s}$ and sum over the data from $p = -M, \dots, M-1$, we obtain (after some reworking of the indices):

$$Q_n^{(s)} \doteq \frac{1}{2M} \sum_{p=-M}^{M-1} Q_n(p) e^{-ip(\pi/M)s} \\ = \sum_{k=\max\{0,-s\}}^{\infty} \mathcal{M}_{nk}^{(s)} \rho_{k,k+s} \quad (6.31)$$

with matrix elements

$$\mathcal{M}_{nk}^{(s)} = \frac{e^{-a^2} |\alpha|^{2n}}{n!} \sum_{j=0}^{\min\{n,k\}} \sum_{j'=0}^{\min\{n,s+l\}} |\alpha|^{2(l-j-j')+s} (-1)^{-j-j'} \\ \times \binom{n}{j} \binom{n}{j'} \frac{\sqrt{(s+n)!n!}}{(s+n-j)!(n-j)!}. \quad (6.32)$$

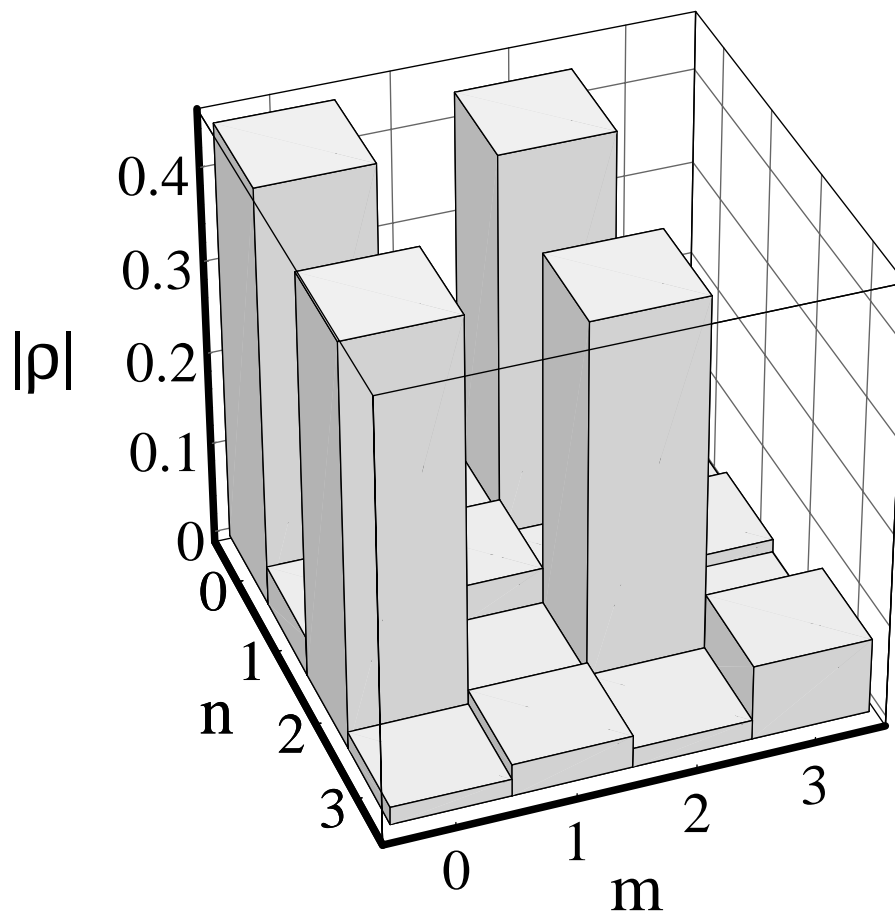


Figure 6.7: Reconstructed density matrix amplitudes of an approximate $\frac{1}{\sqrt{2}}(|n=0\rangle - i|n=2\rangle)$ state.

In practice, we can truncate the infinite sum in Eq. (6.31) at some N . Then we can invert the matrix equation to determine $\rho_{n,m}$, using standard techniques.

Fig. 6.7 shows the reconstructed density matrix element amplitudes (in the Fock-state basis) for an approximate $\frac{1}{\sqrt{2}}(|n=0\rangle - i|n=2\rangle)$ state.

6.4 Quantum State Engineering of Two Ions

Cirac and Zoller’s scheme for quantum computation ([40], see Sec. 7.3) calls for a collection of trapped ions, each of which may be individually addressed by laser beams. Thus far, I have discussed single-ion experiments but obviously, if we wish to work towards a quantum register along the lines of Cirac and Zoller, we need to work with multiple ions. The challenge in this task is to focus laser beams tightly enough to address the ions while simultaneously keeping the trap strong enough to allow easy manipulation of the ions’ motion and minimize the effects of background heating. Of course, these two tasks are at odds with each other: a strong trap forces the ions together, making individual addressing more of a challenge.

We have, indeed, focussed the laser beams down to a waist of $\approx 3 \mu\text{m}$ and addressed one of two trapped ions, with negligible interaction of the other ion with the beams. This was done in the Be-electrode elliptical microtrap, with $\omega_x \approx 6 \text{ MHz}$. However, it was a somewhat challenging task. The AOMs used to switch the beams on and off did not produce ideal, Gaussian beams, and so there was a lot of stray light. This was reduced by sending the beam through a single mode fiber before focussing it through the trap. The fiber, however, added amplitude noise to the light (peaked around several kHz), so that it was necessary to add extra “noise-eater” circuitry to eliminate this noise. Even then, however, it was not possible to achieve high fidelity when the beams were focussed tightly. The coaxial resonator, as it turned out, was also a long mechanical lever arm, which transmitted acoustic and mechanical vibrations from the room and optical table to the trap structure, and caused it to oscillate with respect to the beam waist, reducing the fidelity of laser-induced interactions.

These technical problems are, of course, surmountable in principle. But, in the meantime, we were able to perform interesting multi-particle experiments without hav-

ing to focus the laser beams or reduce the trap strength. In particular, we were able to create entangled states of two ions' spins.

Multi-ion entangled states, such as two-particle Bell states [10, 144] or Greenberger-Horne-Zeillinger triplets [145] ($\frac{1}{\sqrt{2}}[|\downarrow, \downarrow, \downarrow\rangle + |\uparrow, \uparrow, \uparrow\rangle]$), are interesting for the opportunities they provide to test quantum mechanics versus other possible theories [146] and for their illustration of quantum mechanics' seemingly paradoxical nature. But multi-ion entangled states are also of more practical and immediate interest in precision spectroscopy. For such applications, the Ramsey method of separated oscillatory fields [95] (see Sec. 3.4) is generally used to ascertain the frequency of a transition; for example, the frequency of the $|\downarrow\rangle \rightarrow |\uparrow\rangle$ transition in our case. If all sources of technical noise are eliminated, then the fundamental limit to the Ramsey method's accuracy is the "quantum projection noise" [147] from the projection of the atoms onto one or the other basis state during the probe pulse. For uncorellated atoms, this limit is given by $\frac{\delta\omega}{\omega} = \frac{1}{\sqrt{NT_R\tau_I}}$, where T_R is the time between the two Ramsey zones, τ_I is the total averaging time for the complete frequency measurement and N is the number of atoms. On the other hand, if we could replace the first $\frac{\pi}{2}$ pulse with one that produces the state $|\psi_{en}\rangle = \frac{1}{\sqrt{2}}(|\downarrow, \downarrow, \dots, \downarrow\rangle + e^{i\phi}|\uparrow, \uparrow, \dots, \uparrow\rangle)$, then the fundamental precision is given by $\frac{\delta\omega}{\omega} = \frac{1}{N\sqrt{T_R\tau_I}}$, which is the so-called "Heisenberg limit" [148].

6.4.1 Entangled States of Two Ions

The most straightforward way to produce entangled states such as the Bell states⁴ $|\psi_B^\pm\rangle = \frac{1}{\sqrt{2}}(|\downarrow, \uparrow\rangle \pm |\uparrow, \downarrow\rangle)$ is to address the ions differentially. In order to do so, we need some way of introducing a different interaction at each ion. One possibility is to focus the laser beams tightly so that one ion is illuminated while the other is not (i.e., has zero Rabi frequency). However, there is another way to achieve the same effect by using the micromotion.

⁴ Note that $|\psi_B^-\rangle$ is the "Einstein, Podolsky, Rosen" (EPR) pair.

Recall from Sec. 2.1 that a trapped ion's motion is made up of two parts: the slow secular motion at ω_m , which we cool and quantize, and the fast, small amplitude, classical micromotion at Ω_T . This micromotion can “fuzz out” the interaction with the laser beams, thereby reducing the coupling strength. Near the null of the rf trapping field, the amplitude of the micromotion is negligible. However, by applying a static potential to an additional electrode [81], we can shift the two ions such that one is near the rf null point but the other is not. In such a case, the micromotion is different for the two ions and hence so is the coupling to the laser beams [49].

In Eq. (3.4), the micromotion is ignored. To now take it into account, we write the position of the ion as

$$\hat{x}_{tot} = x_\mu + \hat{x} = x_{\mu 0} \cos(\Omega_T t) + x_0(\hat{a}_x^\dagger + \hat{a}_x), \quad (6.33)$$

where $x_{\mu 0}$ is the amplitude of the micromotion along the x -direction (I am considering the x -direction now, as these experiments were performed in one of the elliptical traps). Thus, we may re-express Eq. (3.4) as

$$H'_{int} = \hbar\Omega \left[S_+ e^{i\Delta k \cdot x_{\mu 0} \cos \Omega_T t} \exp\left(i\eta(\hat{a}_x^\dagger e^{i\omega_x t} + \hat{a}_x e^{-i\omega_x t}) - i\delta t\right) + H.C. \right]. \quad (6.34)$$

I have treated the micromotion as classical in Eq. (6.34). Although one may treat the complete motion of the ions quantum-mechanically [70], we still obtain an appropriate picture of the situation without doing so, as we shall see.⁵ Expanding $e^{i\Delta k \cdot x_{\mu 0} \cos \Omega_T t}$ [72], we find that the effect of the micromotion is that the base (carrier) Rabi frequency $\Omega \rightarrow \Omega_j = \Omega J_0(|\delta k| \cdot x_{\mu 0, j})$, where $j \in \{1, 2\}$ is the j^{th} ion. That is, in the case of two trapped ions, the ion with the most micromotion is more weakly coupled to the laser beams, as discussed above. This is illustrated by the data in Fig. 6.8: as the center of mass of the two-ion system is displaced from trap center (by an applied static electric field), the ion which is moved closer to trap center experiences an increased Rabi

⁵ This occurs because $\sqrt{\frac{\hbar}{2m\omega_x}} \ll x_{\mu 0}$

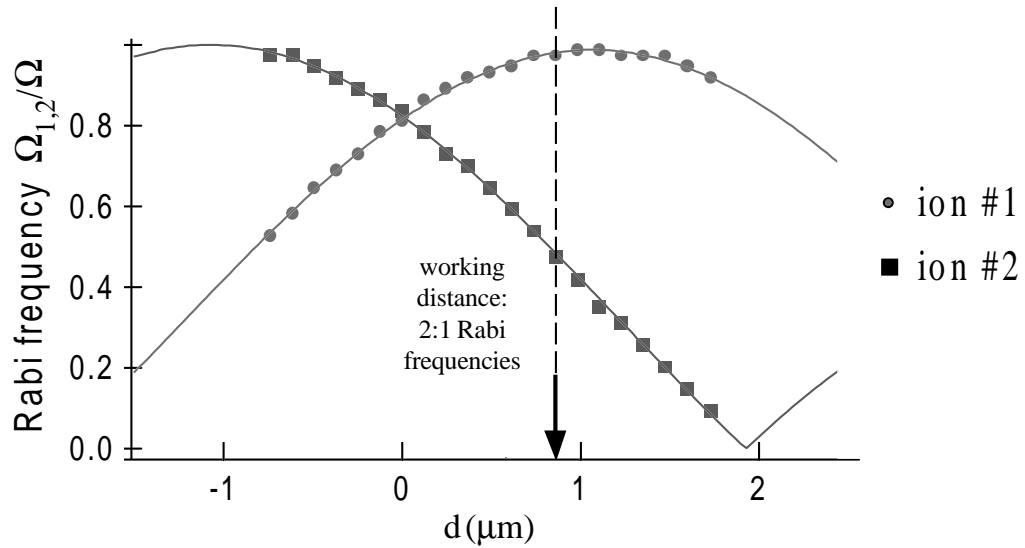


Figure 6.8: Normalized carrier Rabi frequency Ω_i/Ω of each of two ions as a function of center-of-mass displacement d from the rf null position $d=0$. Ω is the co-propagating carrier transition Rabi frequency. The solid curves show $\Omega J_0(|\delta k| \cdot x_{\mu 0, i})$, where the distance between the maxima of the two curves sets the scale of the ordinate, based on the known ion-ion spacing of $l \approx 2.2 \mu\text{m}$ at $\omega_x/2\pi = 8.8 \text{ MHz}$. When the center of the two-ion string is displaced by just under one micrometer from the center of the trap (arrow in graph), the two ions' Rabi frequencies are in a two-to-one ratio.

frequency while the other ion's Rabi frequency is reduced. The agreement with theory is quite good.

Using the micromotion to differentially address the two ions, we have found a way to produce the state

$$|\psi_e(\phi)\rangle = \left(\frac{3}{5} |\downarrow, \uparrow\rangle - e^{i\phi} \frac{4}{5} |\uparrow, \downarrow\rangle \right) |n=0\rangle, \quad (6.35)$$

which has an overlap $|\langle\psi_B^-|\psi_e(\varphi=0)\rangle|^2 = |\langle\psi_B^+|\psi_e(\varphi=\pi)\rangle|^2 = 0.98$ with the Bell states [49]. (In Eq. (6.35), ϕ is a controllable phase, determined by the laser beams' phases at the locations of the two ions.)

To do this, we displaced the ions' center of mass from the trap center to the point indicated by the arrow in Fig. 6.8: at this point the ions' perpendicular carrier Rabi

frequencies were in a 2:1 ratio. Thus, starting from the state $|\psi_i\rangle = |\downarrow, \downarrow, n_{str} = 0\rangle$ we drove a 2π pulse on one ion and a π pulse on the other, creating the state $|\psi'\rangle = |\downarrow, \uparrow, n_{str} = 0\rangle$.

From this point, we were able to use the stretch red sideband to produce the state $|\psi_e(\phi)\rangle$. To see how this occurred, consider the level structure shown in Fig. 6.9, which shows the various states coupled to $|\downarrow, \uparrow, n\rangle$ by the stretch lower motional sideband, and let $\Omega_1 = 2\Omega_2$ be the carrier Rabi frequencies on ions 1 and 2, respectively. Since we started out in $n_{str} = 0$, there is no $n_{str} = n - 1$ level to which to couple. Thus, starting in $|\psi'\rangle$, and driving on the stretch red sideband for a time t_{int} , we produced the state:

$$\begin{aligned} |\psi(t)\rangle &= -\frac{i\Omega_{2-}}{\mathcal{G}} \sin \mathcal{G}t_{int} |\downarrow, \downarrow, 1\rangle \\ &+ \left[\frac{\Omega_{2-}}{\mathcal{G}^2} (\cos \mathcal{G}t_{int} - 1) + 1 \right] |\downarrow, \uparrow, 0\rangle \\ &+ e^{i\phi} \left[\frac{\Omega_{2-} - \Omega_{1-}}{\mathcal{G}^2} (\cos \mathcal{G}t_{int} - 1) \right] |\uparrow, \downarrow, 0\rangle. \end{aligned} \quad (6.36)$$

Here, $\mathcal{G} = \sqrt{\Omega_{2-}^2 + \Omega_{1-}^2}$, $\Omega_{j-} = \Omega_j \eta_{x, str} \sqrt{n+1}$ is the stretch mode red sideband Rabi frequency (recall $\eta_{x, str} = \eta_x / \sqrt{2\sqrt{3}}$), and ϕ is the difference of the Raman beam phases at the ions. Thus, when $\mathcal{G}t_{int} = \pi$, we produced the state $|\psi_e(\phi)\rangle$. Since the laser beams impinge on the ions at an angle to the axis along which they line up, the phase ϕ depends on the ions' separation. Thus, by changing this separation, we could choose the particular state produced.

By monitoring the photon-number histograms (Ch. 3 and Appendix A), we could discriminate between $|\downarrow, \downarrow\rangle$, $|\downarrow, \uparrow\rangle$, $|\uparrow, \downarrow\rangle$, and $|\uparrow, \uparrow\rangle$, and extract the spin populations for the state which we produce. The optical pumping of the dark state $|\uparrow\rangle$ into the cycling transition (Appendix A) somewhat complicated this endeavour. Were it not for this effect, we could have turned up the intensity of D2 to a point where the photon histograms allowed us to clearly distinguish between the cases $|\downarrow, \downarrow\rangle$, $|\uparrow, \downarrow\rangle$ or $|\downarrow, \uparrow\rangle$,⁶ and $|\uparrow, \uparrow\rangle$. However, the optical pumping precluded this. Instead, we took

⁶ Note that, due to the different micromotions of the two ions, these two states had different scatter rates during the cycling transition

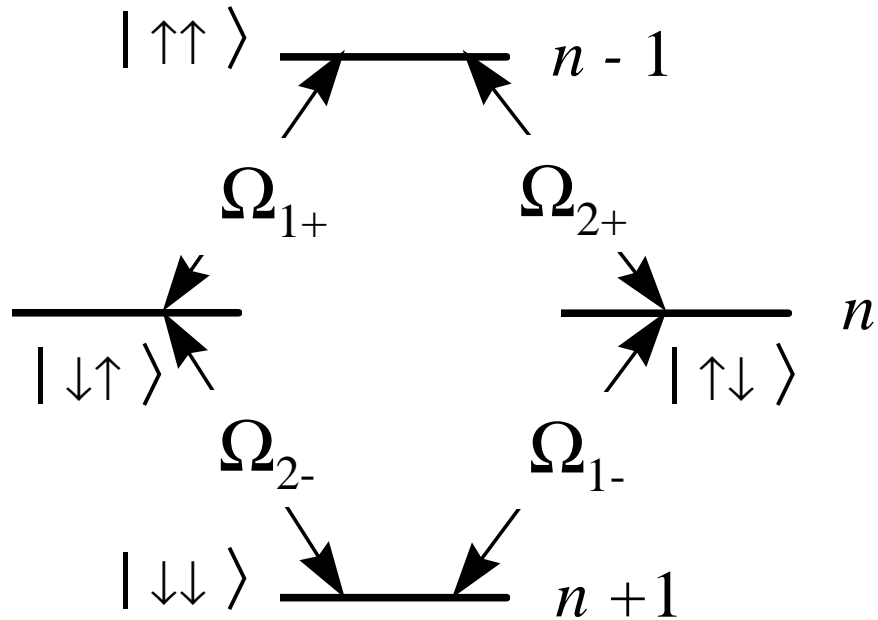


Figure 6.9: Simplified level diagram showing four levels coupled by the lower (red) motional sideband, when the lasers illuminate two trapped ions. The coupling strengths, $\Omega_{j,\pm}$, vary depending on which ion’s spin is being flipped, due to the ions’ different (micromotion-induced) base Rabi frequencies (see Eq. (6.36)).

“reference histograms” for the four states (see Fig. 6.10), and performed a singular-valued decomposition [96] of the measured fluorescence signal using these references as basis functions.

In order to demonstrate the coherence of the produced state, we applied the co-propagating carrier. To determine the effect of this interaction on the Bell states, it is useful to again draw the analogy between two-level systems and spin-1/2 particles. In particular, we may split the possible two-ion coupled spin states into a triplet and a singlet manifold, just as one does when treating two, coupled spin-1/2 systems. The singlet, which has spin $J = 0$, should be unaffected by any interaction which preserves

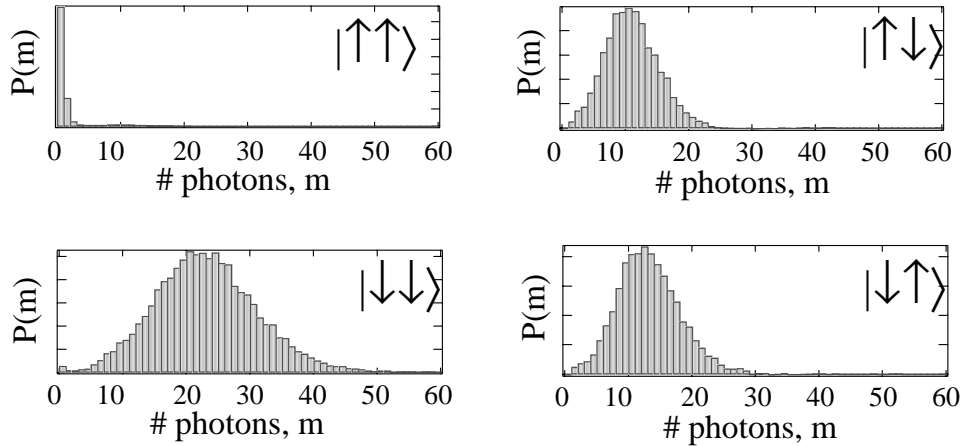


Figure 6.10: Photon-number histograms for two trapped ions. Since the ions were unequal distances from the rf null, and experience different micromotions, the mean photon numbers for the states $|\uparrow, \downarrow\rangle$ and $|\downarrow, \uparrow\rangle$ were different (see text). The “leak” of population from $|\uparrow\rangle$ into the cycling transition is discussed in Appendix A.

J. An example of such an interaction is the co-propagating carrier which, being insensitive to motion, does not “sense” the micromotion and so interacts with both ions with the same coupling strength. On the other hand, the states $|\psi_B^\pm\rangle \approx |\psi_e(0)\rangle$ or an incoherent mixture of $|\downarrow, \uparrow\rangle$ and $|\uparrow, \downarrow\rangle$ are driven to the states $|\uparrow, \uparrow\rangle$ and $|\downarrow, \downarrow\rangle$ by the co-propagating carrier. Thus, measuring the photon statistics after turning on the co-propagating carrier allowed us to distinguish between the coherent superposition $|\psi_e(\pi)\rangle$ and an incoherent mixture. The data are shown in Fig. 6.11. Together with the population analysis described above, they establish that we were able to create the desired state $|\psi_e(\phi)\rangle$ about 70% of the time [49].

Note that it is, in fact, possible to *exactly* produce the Bell states. This would require $\Omega_1 = (\sqrt{2}+1)\Omega_2$ for the red sideband interaction, Eq. (6.36), which would create the exact Bell state from $|\downarrow, \uparrow, 0\rangle$. In practice, it was not possible to change the ratio of the Rabi frequencies within the course of a single experiment, and so the technique

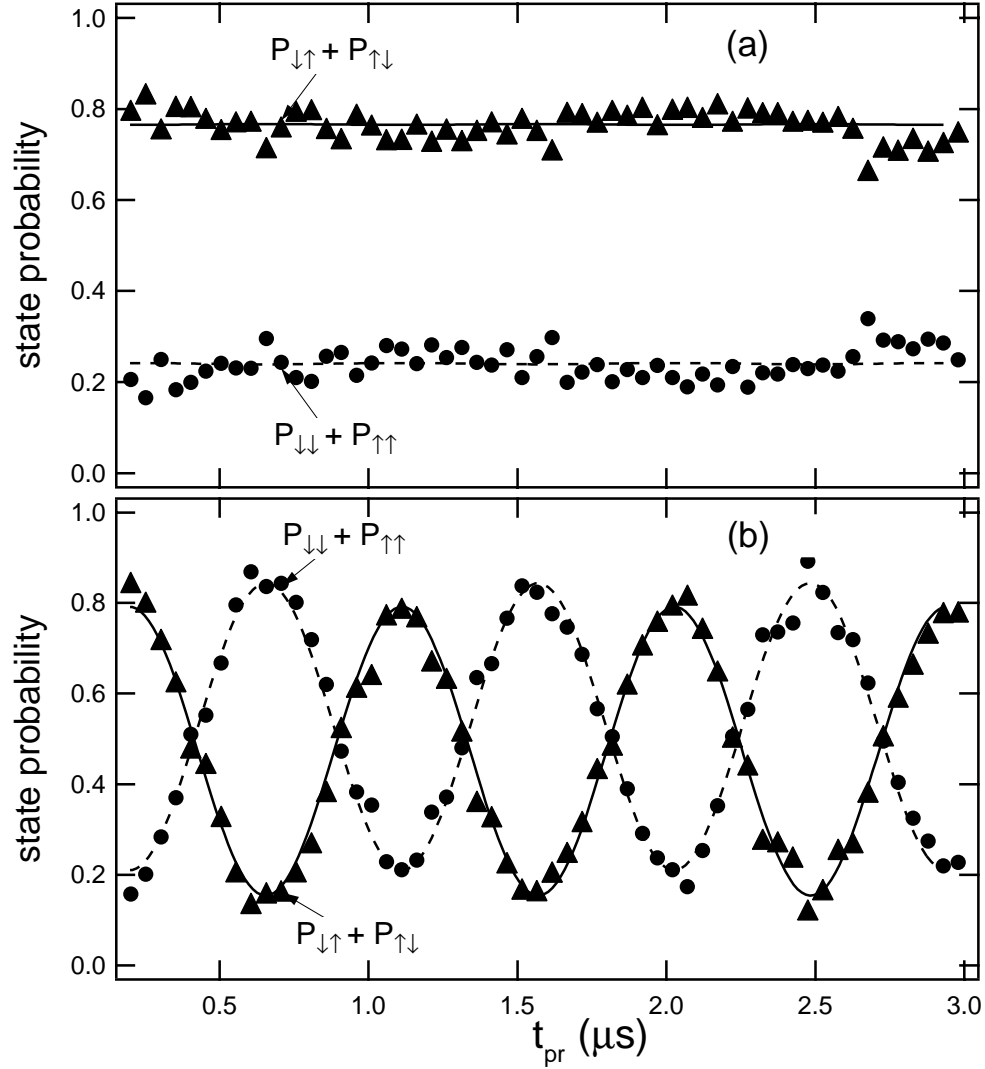


Figure 6.11: Probabilities $P_{\downarrow,\uparrow} + P_{\uparrow,\downarrow}$ and $P_{\downarrow,\downarrow} + P_{\uparrow,\uparrow}$ as a function of pulse length t_{pr} of the co-propagating carrier pulse applied after creation of the state $|\psi_e(\phi)\rangle$ of Eq. (6.35). (a) For $\phi = \pi$, this co-propagating carrier pulse has no effect. (b) For $\phi = 0$, the co-propagating carrier pulse causes the various populations to change. An *incoherent* mixture would also exhibit oscillations. The data in (a) for $\phi = \pi$ thus indicates our success in producing a coherent superposition state. The solid and dashed lines in (a) and (b) are sinusoidal fits to the data, from which we determine that we produce the desired state with a fidelity of $|\langle\psi_{actual}|\psi_e\rangle|^2 = 0.70$.

described above was used, instead. However, this technical difficulty is, in principle, surmountable. For example, we could change the ion-ion separation by changing the trap frequency of a linear trap in the middle of an experiment (see Sec. 7.5).

We note that, in contrast to previous experiments which have produced entangled states (see references in [49]), this present technique is *deterministic* [149]. That is, it allows production of a known and controllable quantum state of (all of) a particular set of particles, generated at a specified time. Such deterministic entanglement, along with the ability to store the states so produced, is crucial for large-scale quantum computation.

6.4.2 Creating Multi-Ion Entangled States

The techniques discussed in the last section are useful for producing Bell-type states. However, they are not readily scalable to more than two ions. Sørensen and Mølmer [150] have proposed a scheme to produce maximally-entangled states which *is* scalable to multiple ions. It is also relatively insensitive to heating of the ions' motion, so long as the ions remain in the Lamb-Dicke regime.

This scheme requires one to illuminate all the ions simultaneously with the blue and red motional sidebands. The original proposal dealt with a two-photon coupling in a situation where, for example, the carrier would be driven by a single-photon interaction. In our case, where the carrier and motional sidebands are driven by two-photon transitions, Sørensen and Mølmer's scheme would require four-photon transitions. This does not change the basic physical principles of the technique. So, for the sake of simplicity, I shall use their original case to sketch out the idea of the method.

In order to understand how the technique works, consider the case of two ions. The situation is sketched out in Fig. 6.12. Here, two ions start out in the state $|\downarrow, \downarrow, n\rangle$. Two laser beams illuminate the ions. One is tuned to $\omega_0 + \varepsilon$, where $\varepsilon \approx \omega_x$ but $\varepsilon \neq \omega_x$ (i.e. the levels $|\downarrow, \uparrow, n-1\rangle$ and $|\uparrow, \downarrow, n-1\rangle$ are used as virtual levels). The other laser is tuned to $\omega_0 - \varepsilon$. The basic idea of the scheme is that four different two-photon

paths exist connecting $|\downarrow, \downarrow, n\rangle$ and $|\uparrow, \uparrow, n\rangle$: two which “go through” a virtual level with $n + 1$ phonons and two through a virtual level with $n - 1$ phonons. In the Lamb-Dicke regime, the paths which “pass through” the level $|n + 1\rangle$ have coupling strengths $(\sqrt{n + 1}\Omega\eta)^2/(\varepsilon - \omega_x)$ whereas those passing through the $|n - 1\rangle$ have coupling strengths $(\sqrt{n}\Omega\eta)^2/(\omega_x - \varepsilon)$ (notice the difference in sign). When the amplitudes corresponding to the four paths are added up, the n -dependent terms cancel out, leading to an overall coupling strength

$$\Omega_{eff} = \frac{\eta^2\Omega^2\omega_x}{2(\omega_x^2 - \varepsilon^2)}. \quad (6.37)$$

Thus, the levels $|\downarrow, \downarrow, n\rangle$ and $|\uparrow, \uparrow, n\rangle$ are coupled, with no coupling to any other levels. In particular, levels with different n do not mix (although there is some negligible probability that the levels used as “virtual levels” will be populated — this is similar to the case considered in Sec. 3.3). So, as long as the ion is in the Lamb-Dicke regime, this scheme provides a way to make the Bell states, without requiring ground-state laser cooling. Furthermore, the technique works for an arbitrary number of ions.⁷ For multiple ions, spin-flip transitions are driven between all possible pairs of spins, and this realizes the desired time evolution [151].

In order to implement this technique experimentally, we added a second double-pass AOM to the Red Raman beam line (see Ch. 4) so that, with the micromachined linear trap, we could illuminate two trapped ions on their upper and lower stretch sidebands at the same time. However, since the interaction strength was proportional to η^2 , the interaction times necessary to realize Bell states were quite long. We ran into problems with fluctuating magnetic fields and with Debye-Waller factors [73] due to heating of the COM mode: these issues made it quite challenging to realize the coupling of Eq. (6.37) in a coherent fashion. As we were attempting to deal with these issues, the two-ion lifetime went down in a dramatic fashion. We hope to attempt the experiments again in a newly constructed linear trap.

⁷ For an odd number of ions, an additional carrier pulse is required.

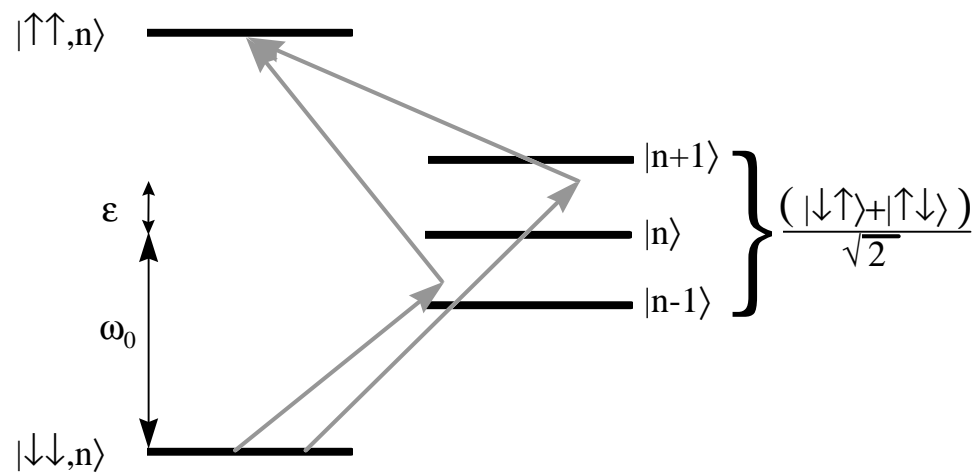


Figure 6.12: Schematic of the two-photon interaction proposed by Sørensen and Mølmer to produce maximally entangled states (two-ion case). The ions are equally illuminated by two lasers, of frequencies $\omega_0 \pm \epsilon$, where $\epsilon \approx \omega_x$ but $\epsilon \neq \omega_x$. The two ions' energy levels are shown in the triplet/singlet representation, and only the triplet levels are shown (since the singlet does not couple to the lasers). Two paths between $|\downarrow, \downarrow, n\rangle$ and $|\uparrow, \uparrow, n\rangle$ are possible: one path uses $|(\uparrow\downarrow + \downarrow\uparrow), n+1\rangle$ as a virtual level, whereas the other path uses $|(\uparrow\downarrow + \downarrow\uparrow), n-1\rangle$. The n -dependencies of the two paths cancel out, allowing creation of maximally entangled states.